Monthly Notices
of the
ROYAL ASTRONOMICAL SOCIETY

MNRAS **497,** 2340–2351 (2020)
Advance Access publication 2020 July 11

doi:10.1093/mnras/staa2034

ExoMol line lists – XL. Rovibrational molecular line list for the hydronium ion (H_3O^+)

S. N. Yurchenko,[1] Jonathan Tennyson,[1★] Steve Miller,[1] V. V. Melnikov,[2] J. O'Donoghue[3] and L. Moore[4]

[1] *Department of Physics and Astronomy, University College London, Gower Street, WC1E 6BT London, UK*
[2] *Siberian Institute of Physics & Technology, Tomsk State University, Tomsk 634050, Russia*
[3] *JAXA Institute of Space and Astronautical Science, Sagamihara City, Kanagawa Prefecture, 252-5210 Japan*
[4] *Center for Space Physics, Boston University, Boston, 02215 MA, USA*

Accepted 2020 July 7. Received 2020 June 25; in original form 2020 May 5

ABSTRACT

A new line list for hydronium ($H_3{}^{16}O^+$) is computed. The line list is based on a new *ab initio* dipole moment surface (CCSD(T)/aug-cc-pVQZ) and a new empirical potential energy surface (PES). The empirical PES of H_3O^+ was obtained by refining an *ab initio* surface through a global fit to the experimentally determined rovibrational energies collected from the literature covering the ground, $\nu_1^{\pm}$, $\nu_2^{\pm}$, $2\nu_2^{\pm}$, $\nu_3^{\pm}$, and $\nu_4^{\pm}$ vibrational states. The line list covers the wavenumber range up to 10 000 cm^{-1} (wavelengths > 1 μm) and should be complete for temperatures up to $T = 1500$ K. This is the first comprehensive line list for H_3O^+ with extensive wavenumber coverage and accurate transitional probabilities. Prospects of detection of hydronium in spectra of Solar system giant planets as well as exoplanets are discussed. The eXeL line list is publicly available from the ExoMol and CDS data bases.

Key words: molecular data – astronomical data bases: miscellaneous – planets and satellites: atmospheres – planets and satellites: gaseous planets.

1 INTRODUCTION

Hydronium and its isotopologues play an important role in planetary and (inter)stellar chemistry (Dalgarno & Black 1976; Jensen et al. 2000; Goicoechea & Cernicharo 2001; Gerin et al. 2010; Hollenbach et al. 2012; González-Alfonso et al. 2013; Indriolo et al. 2015; Sánchez Contreras et al. 2015; Tran et al. 2018; Martinez et al. 2019). These ions are found to exist abundantly in both diffuse and dense molecular clouds (Hollis et al. 1986; Wootten et al. 1986, 1991; Phillips, van Dishoeck & Keene 1992; Timmermann et al. 1996; Goicoechea & Cernicharo 2001; Gerin et al. 2010; Hollenbach et al. 2012; González-Alfonso et al. 2013; Indriolo et al. 2015) as well as in comae (Rubin et al. 2009). H_3O^+ is an indicator of the presence of water and can be used to estimate H_2O abundances when the direct detection is unfeasible (Phillips et al. 1992; Roy & Dang 2015). H_3O^+ was detected in comets Hale–Bopp and Halley (Balsiger et al. 1986; Lis et al. 1997; Mehringer et al. 1997; Rauer 1997). Observations of H_3O^+ are one of the approaches to establish interstellar concentrations of H_2O. Dissociative recombination of H_3O^+ with electrons is thought to be the main source for the synthesis of water dense interstellar clouds (Millar et al. 1988; Wootten et al. 1991; Andersen et al. 1996) and may lead to formation of a population of vibrationally hot water in comets (Barber et al. 2007).

H_3O^+ is expected to exist in a wide variety of environments, such as diffuse interstellar clouds, at very low temperatures or, for example, the atmospheres of giant planets (Moore et al. 2018), brown dwarfs, and cool stars that are significantly hotter. Recent laboratory experiments by Bourgalais et al. (2020) suggest the H_3O^+ is likely to be both the dominant and the most easily observed molecular ions in sub Neptune exoplanets; Bourgalais et al. (2020) also suggest that H_3O^+ should be observable by forthcoming exoplanet characterization space missions, such a detection would require a reliable line list for hot H_3O^+. Helling & Rimmer (2019) suggest that H_3O^+ should be detectable in free-floating brown dwarfs and superhot giants.

Dissociative recombination of hydronium H_3O^+ has been extensively studied in ion storage rings by Andersen et al. (1996), Neau et al. (2000), Jensen et al. (2000), Buhr et al. (2010), and Novotny et al. (2010). The sensitivity of the Hydronium spectrum to variations of the electron-to-proton mass ratio was studied by Kozlov & Levshakov (2010) and Owens et al. (2015).

The H_3O^+ ion is destroyed primarily by electrons and ammonia (Helling & Rimmer 2019). H_3O^+ is one of the species used in the spectroscopic breath analysis (Spanel, Spesyvyi & Smith 2019).

Hydronium (H_3O^+) is a pyramidal molecule characterized by an umbrella motion with a very low barrier to the planarity of around 650.9 cm^{-1} (Rajamäki et al. 2004). As a result, vibrational ground state is split due to tunnelling by 55.35 cm^{-1} (Tang & Oka 1999), significantly more than in the isoelectronic ammonia molecule.

★ E-mail: j.tennyson@ucl.ac.uk

Published by Oxford University Press on behalf of the Royal Astronomical Society

Theoretical studies of structure, inversion barrier, and rovibrational energy levels of H_3O^+ were carried out by Lischka & Dyczmons (1973), Ferguson & Handy (1980), Špirko & Bunker (1982), Botschwina, Rosmus & Reinsch (1983), Liu, Oka & Sears (1986), and Yurchenko, Bunker & Jensen (2005a). The electronic structure of hydronium and hydronium–water clusters was studied by Ermoshin, Sobolewski & Domcke (2002).

Accurate *ab initio* studies include works by Chaban, Jung & Gerber (2000), Rajamäki, Miani & Halonen (2003), Huang, Carter & Bowman (2003), Rajamäki et al. (2004), Mann et al. (2013), Owens et al. (2015), and Yu & Bowman (2016), where potential energy surface (PES) and dipole moment surface (DMS) of H_3O^+ were computed using high levels of theory.

Chemistry of H_3O^+ was also a subject of numerous studies (Hollenbach et al. 2012; Roy & Dang 2015; Cranfield et al. 2016). The influence of the liquid environment on the spectroscopic properties of H_3O^+ was studied by Tan et al. (2016).

Experimental data on the high-resolution line positions of H_3O^+ were collected by Yu et al. (2009) from a large set of high-resolution spectroscopy studies (Begemann et al. 1983; Bunker, Amano & Špirko 1984; Davies, Johnson & Hamilton 1984; Hasse & Oka 1984; Lemoine & Destombes 1984; Begemann & Saykally 1985; Bogey et al. 1985; Liu & Oka 1985; Plummer, Herbst & De Lucia 1985; Sears et al. 1985; Davies et al. 1986; Gruebele, Polak & Saykally 1987; Stahn et al. 1987; Haese, Liu & Oka 1988; Verhoeve et al. 1988; Verhoeve et al. 1989; Okumura et al. 1990; Petek et al. 1990; Ho, Pursell & Oka 1991; Uy, White & Oka 1997; Araki, Ozeki & Saito 1999; Tang & Oka 1999; Stephenson & Saykally 2005; Dong & Nesbitt 2006; Rui et al. 2007; Furuya & Saito 2008; Yu et al. 2009; Müller et al. 2010; Petit, Wellen & McCoy 2012). Yu et al. (2009) used these data in a global spectroscopic analysis with the SPFIT/SPCAT effective Hamiltonian approach (Pickett 1991), together the H_3O^+ line positions from NASA JPL (Pickett et al. 1998). They have computed a set of empirical energies of H_3O^+ for $J = 0, \dots, 20$ for the ground as well as the $\nu_1^\pm$, $\nu_2^\pm$, $2\nu_2^\pm$, $\nu_3^\pm$, and $\nu_4^\pm$ vibrational states. We use these energies to refine our spectroscopic data.

In our recent work on H_3O^+ (Melnikov et al. 2016), we computed a low-temperature line list for all main isotopologues of H_3O^+ using the *ab initio* PES and DMS of Owens et al. (2015) combined with accurate variational nuclear motion calculations using TROVE (Yurchenko, Thiel & Jensen 2007), where accurate lifetimes of these ions were reported. Here, we present a new hot line list for the main isotopologue of H_3O^+ generated using a new *ab initio* DMS (CCSD(T)/aug-cc-pVQZ), a new spectroscopic PES, and the program TROVE. This work is performed as part of the ExoMol project that provides molecular line lists for exoplanet and other atmospheres (Tennyson & Yurchenko 2012).

2 POTENTIAL ENERGY SURFACE

The PES was represented by a Taylor-type expansion of eighth order

$$V(r_1, r_2, r_3, \alpha_{12}, \alpha_{13}, \alpha_{23}) = \sum_{i_1, i_2, i_3, i_2, i_3, i_6} f_{i_1, i_2, i_3, i_2, i_3, i_6} \chi_1^{i_1} \chi_2^{i_2} \chi_3^{i_3} \chi_4^{i_4} \chi_5^{i_5} \chi_6^{i_6} \tag{1}$$

using the following definition of the expansion coordinates:

$$\chi_k = 1 - \exp\left[-a(r_k - r_e)\right], \quad (k = 1, 2, 3), \tag{2}$$

$$\chi_4 = (2\alpha_{23} - \alpha_{13} - \alpha_{12}) / \sqrt{6}, \tag{3}$$

$$\chi_5 = (\alpha_{13} - \alpha_{12}) / \sqrt{2}, \tag{4}$$

$$\chi_6 = \sin \bar{\rho} = \frac{2}{\sqrt{3}} \sin\left[(\alpha_{23} + \alpha_{13} + \alpha_{12})/6\right], \tag{5}$$

where r_1, r_2, and r_3 are the three bond lengths, α_{12}, α_{13}, and α_{23} are the three inter-bond angles, and umbrella mode $\bar{\rho}$ is an angle between a symmetric C_3 axis and molecular bonds r_i for a reference structure defined by the mean angle $\bar{\alpha}$:

$$\bar{\alpha} = \frac{1}{3}(\alpha_{23} + \alpha_{13} + \alpha_{12}).$$

The potential energy function $V(r_1, r_2, r_3, \alpha_{12}, \alpha_{13}, \alpha_{23})$ of H_3O^+ must be fully symmetric and transform as A_1' of $\mathcal{D}_{3h}$(M). Therefore, the potential parameters $f_{i_1, i_2, i_3, i_4, i_5, i_6}$ are related through the corresponding symmetry properties of A_1'. Here, we use the same symmetry-adapted expansion of the potential energy function as developed for ammonia in Yurchenko et al. (2005b).

3 DIPOLE MOMENT SURFACE

A new high-level *ab initio* DMS of H_3O^+ was computed with MOLPRO (Werner et al. 2012) using the CCSD(T)/aug-cc-pVQZ level of theory (coupled cluster with all single and double excitations and a perturbational estimate of connected triple excitations) and the augmented correlation consistent quadruple zeta basis set (Dunning 1989; Kendall, Dunning & Harrison 1992; Woon & Dunning 1993; Dunning, Peterson & Wilson 2001), in the frozen core approximation. The three components of the electronically averaged dipole moment $\bar{\mu}$ of H_3O^+ were obtained as finite difference derivatives with respect to a weak (0.002 au) external field on a grid of 26 271 geometries covering the energy range up to $hc \cdot 23\,000$ cm^{-1} with the bond lengths and bond angles varying as 0.96–1.3 Å and 70–125°, respectively. These three DMSs were then represented analytically using the symmetrized molecular bond (SMB) representation of Yurchenko et al. (2009). In this representation, the dipole moment vector $\bar{\mu}$ is given by symmetrized projections on to the molecular bonds with the dipole moment components $(\overline{\mu}_{A_2''}, \overline{\mu}_{E_a'}, \overline{\mu}_{E_b'})$ in the molecule fixed axis system given by sixth-order polynomial expansions

$$\bar{\mu}_{\Gamma}(r_1, r_2, r_3, \alpha_{12}, \alpha_{13}, \alpha_{23}) = \sum_{i_1, i_2, i_3, i_2, i_3, i_6} \mu^{\Gamma}_{i_1, i_2, i_3, i_2, i_3, i_6} \zeta_1^{i_1} \zeta_2^{i_2} \zeta_3^{i_3} \zeta_4^{i_4} \zeta_5^{i_5} \zeta_6^{i_6}, \tag{6}$$

where $\Gamma = A_2''$, E_a', and E_b' are the irreducible components of $\mathcal{D}_{3\mathrm{h}}$(M) (Bunker & Jensen 1998),

$$\zeta_k = (r_k - r_{\mathrm{ref}}) \exp\left[-(r_k - r_{\mathrm{ref}})\right], \quad (k = 1, 2, 3) \tag{7}$$

$$\zeta_4 = (2\alpha_{23} - \alpha_{13} - \alpha_{12}) \sqrt{6}, \tag{8}$$

$$\zeta_5 = (\alpha_{13} - \alpha_{12}) / \sqrt{2}, \tag{9}$$

$$\zeta_6 = \sin \bar{\rho}. \tag{10}$$

$\mu^{\Gamma(s)}_{ij\ldots}$ are the expansion parameters, r_{ref} is a reference bond length used as an expansion centre, and $\sin \bar{\rho}$ is the same as in equation (5). The dipole moment expansion parameters are obtained in a least-squares fit to the *ab initio* values. The dipole moment components $(\overline{\mu}_{E_a'}, \overline{\mu}_{E_b'})$ are transformed as linear combinations of each other according with the irreducible representation $E^{'}$ of $\mathcal{D}_{3\mathrm{h}}$(M). In the symmetry-adapted form of Yurchenko et al. (2009) used here, the parameters $(\mu^{E_a(s)}_{ij\ldots}, \mu^{E_b(s)}_{ij\ldots})$ are shared between these two components and thus must be fit together, while $\mu^{A_1(s)}_{ij\ldots}$ are obtained separately (see Yurchenko et al. 2009).

Since the dipole moments of ions depend on the origin of the coordinate, for variational calculations the *ab initio* DMS of H_3O^+ had to be transformed from the coordinate system centred on the oxygen atom used in the MOLPRO calculations to the centre of mass (CM) $\bar{\mu}^{(\mathrm{CM})}_{\alpha}$ as follows:

$$\bar{\mu}^{(\mathrm{CM})}_{\alpha} = \bar{\mu}^{(\mathrm{O})}_{\alpha} - R^{(\mathrm{CM})}_{\alpha} Q,$$

where $R^{(\mathrm{CM})}_{\alpha}$ are the Cartesian coordinates of the centre of mass of H_3O^+ in the old coordinate system and $Q = 4.803206798$ Debye/Å is the charge of the ion in Debye/Å.

The final *ab initio* dipole moment functions (DMFs) required 221 parameters and reproduced the *ab initio* data with an root-mean-squares (rms) error of 0.014 D for geometries with energies up to $hc \cdot 24\,000$ cm^{-1} and 0.00036 D for geometries with energies up to $hc \cdot 12\,000$ cm^{-1}. The *ab initio* DMF of H_3O^+ is included in the supplementary material as a Fortran 90 routine.

Using our *ab initio* (CM) dipole moment and the TROVE vibrational eigenfunctions (see below), we obtained a transition dipole moment for the inversion $0^- \leftrightarrow 0^+$ band of 1.438 D, which coincides with the *ab initio* value of Botschwina et al. (1983) adopted by the CDMS data base (Endres et al. 2016) as the ground state permanent dipole moment.

4 TROVE SPECIFICATIONS

Owing to the low barrier, the rovibrational motion of H_3O^+ is described by the $\mathcal{D}_{3\mathrm{h}}$(M) molecular symmetry group (Bunker & Jensen 1998). For this work, we use a similar set-up to that adopted by Owens et al. (2015) and Melnikov et al. (2016). The kinetic energy operator was constructed as a sixth-order expansion in terms of five rectilinear linearized coordinates $\xi_i^{\mathrm{lin}} = \{\Delta r_1^{\mathrm{lin}}, \Delta r_2^{\mathrm{lin}}, \Delta r_3^{\mathrm{lin}}, S_A^{\mathrm{lin}}, S_B^{\mathrm{lin}}\}$ around a non-rigid configuration following the Hougen–Bunker–Johns approach (Hougen, Bunker & Johns 1970) as implemented in TROVE. These coordinates are linearized versions of the geometrically defined coordinates ξ_i $(i = 1, \ldots, 5)$, constructed from the valence coordinates r_1, r_2, r_3, α_{12}, α_{13}, and α_{23} as follows:

$$\xi_1 = r_1 - r_{\mathrm{e}}, \tag{11}$$

$$\xi_2 = r_2 - r_{\mathrm{e}}, \tag{12}$$

$$\xi_3 = r_3 - r_{\mathrm{e}}, \tag{13}$$

$$\xi_4 = \frac{1}{\sqrt{6}} (2\alpha_{23} - \alpha_{13} - \alpha_{12}), \tag{14}$$

$$\xi_5 = \frac{1}{\sqrt{2}} (\alpha_{13} - \alpha_{12}), \tag{15}$$

where r_{e} is the bond length of H_3O^+. The sixth, inversion coordinate τ is defined as an angle between any of the bonds and their trisector $\mathbf{n}$.

The 1D primitive vibrational basis functions $\phi_{v_i}(\xi_i^{\mathrm{lin}})$ $(i = 1 \ldots 5)$ and $\phi_6(\tau)$ were defined as follows. We used a numerically generated based set for the stretching modes using the Numerov–Cooley approach (Noumerov 1924; Cooley 1961), where 1D stretching Schrödinger equations were solved on a grid of 2000 points r_i^{lin} ranging from 0.4 to 2.0 Å. 1D Harmonic oscillator functions were used to form the bending basis sets for ξ_4 and ξ_5. The inversion basis set was also constructed using the Numerov–Cooley approach on a grid of 8000 τ points ranging from $-55°$ to $55°$. The stretching primitive basis functions $\phi_{v_i}(\xi_i^{\mathrm{lin}})$ $(i = 1, 2, 3)$ were selected to cover $v_i = 0 \ldots 9$, while the excitations of the bending and inversion basis functions extended to $v_i = 36$ ($i = 4, 5, 6$). 1D Hamiltonians for each mode used for the stretching and inversion 1D problems were constructed from the 6D Hamiltonian by setting all other coordinates to their equilibrium values.

TROVE uses a two-step basis set optimization scheme designed to improve the sum-of-product form of the vibrational basis set, see Yurchenko, Yachmenev & Ovsyannikov (2017). At step 1, three sets of reduced Hamiltonian problems are solved for (i) the subgroup of three stretching modes, (ii) the subgroup of two bending modes, and (iii) the inversion mode. These subgroups are organized to form symmetry independent modes so that the eigenfunctions of the corresponding reduced Hamiltonians can be symmetrized and classified according with $\mathcal{D}_{3\mathrm{h}}$(M) using the TROVE automatic symmetrization procedure (Yurchenko et al. 2017). The three reduced Hamiltonians are given by

$$\begin{aligned}\hat{H}^{(1)}_{\mathrm{str}}(\xi_1^{\mathrm{lin}}, \xi_2^{\mathrm{lin}}, \xi_3^{\mathrm{lin}}) &= \langle 0_4|\langle 0_5|\langle 0_6|\hat{H}^{6\mathrm{D}}|0_6\rangle|0_5\rangle|0_4\rangle,\\ \hat{H}^{(2)}_{\mathrm{bnd}}(\xi_4^{\mathrm{lin}}, \xi_5^{\mathrm{lin}}) &= \langle 0_1|\langle 0_2|\langle 0_3|\langle 0_6|\hat{H}^{6\mathrm{D}}|0_6\rangle|0_3\rangle|0_2\rangle|0_1\rangle,\\ \hat{H}^{(3)}_{\mathrm{inv}}(\rho) &= \langle 0_1|\langle 0_2|\langle 0_3|\langle 0_4|\langle 0_5|\hat{H}^{6\mathrm{D}}|0_5\rangle|0_4\rangle|0_3\rangle|0_2\rangle|0_1\rangle.\end{aligned} \tag{16}$$

The final vibrational basis set is a direct product of the corresponding three basis sets. This product is contracted using the following polyad-number condition:

$$P = 4(v_1 + v_2 + v_3) + 2(v_4 + v_5) + v_6 \leq P_{\max} = 36.$$

Once the vibrational part is solved, the eigenfunctions of the $J = 0$ Hamiltonian are contracted again using the condition $\tilde{E}_i \leq 20\,000$ cm^{-1} and used to form our final rovibrational basis as a product with the rotational basis functions. The latter are chosen as the symmetrized rigid rotors wavefunctions (see Yurchenko et al. 2007). The vibrational ($J = 0$) contracted basis set comprised 9134 functions. Using this basis set, for each value of J from 0 to 40, four symmetry-adapted Hamiltonian matrices (A_2', E', A_2'', and E'') were constructed and diagonalized to obtained energies and eigenvectors up to $\tilde{E} = 18\,000$ cm^{-1}. The A_1' and A_1'' eigenfunctions correspond to non-physical representations with the nuclear statistical weights g_{ns} equal zero. The A_2 and E-type symmetries have nuclear statistical weights of 4 and 2, respectively.

The rovibrational states of H_3O^+ were assigned the TROVE quantum numbers (QNs) J, K, v_1, v_2, ...v_6 as well the symmetry labels Γ_{vib} and Γ_{rot} using the largest eigen-contribution from the primitive or contracted basis functions. For spectroscopic applications, we also provide the standard normal mode QNs n_1, n_2, n_3, l_3, n_4, l_4 reconstructed by correlating them to v_1, v_2, ...v_6. Here, n_1 is the symmetric (A_1') stretching QN, respectively; n_2 is the inversion QN (A_2''); n_3 and n_4 are asymmetric (E') stretching and bending QNs, respectively, and l_3 and l_4 are the corresponding vibrational angular momentum QNs. The latter satisfy the standard 2D isotropic oscillator conditions (Bunker & Jensen 1998)

$$l_i = v_i, v_i - 2, \ldots, 0(1).$$

These QNs were estimated as eigenvalues of the vibrational angular momentum operator squared L_z^2 on the primitive bending basis functions $\phi_{v_3}(\xi_3^{\mathrm{lin}})$ and $\phi_{v_4}(\xi_4^{\mathrm{lin}})$ following the methodology described in Coles et al. (2019).

In order to improve the quality of the calculated energies and the line list positions of H_3O^+, an empirical PES of H_3O^+ has been constructed by refining *ab initio* PES of H_3O^+ of Owens et al. (2015) to the available laboratory spectroscopic data. In this fits, we used the empirical H_3O^+ energies collected by Yu et al. (2009), which were constructed as a global fit to the experimental line positions from the literature (see Introduction for the detailed references) using SPFIT/SPCAT (Pickett 1991). Their analysis covered the pure rotational as well as the ν_1, ν_2, $2\nu_2$, ν_3, and ν_4 vibrational states. Our fitting set comprised of energies for $J = 0$, 1, 2, 3, 4, 6, 8, 10, and 16 and is illustrated in Table 1, which also shows the quality of the energies obtained with the refined PES. A few states are found with large or very large residuals (>20 cm^{-1}), which we believe are outliers of the SPFIT/SPCAT analysis.

Due to the limited coverage of the experimental information, the refined PES is still largely based on the initial *ab initio* surface thus affecting the accuracy of the fit and the quality of the energies and line positions extrapolated outside the experimental set, especially for higher excitations corresponding to large distortions of PES. Another source of the inaccuracy is from the non-exact kinetic energy operator (KEO) formalism used in the variational calculations (see Yurchenko et al. 2007) mostly affecting energies at high Js. The KEO errors are usually much smaller (10–100 times) than the errors associated with the *ab initio* character of PES. Even with these caveats, we believe that our results represent a significant improvement to the existing knowledge of the hydronium spectroscopy especially at higher vibrational or rotational excitations.

The potential parameters $f_{i_1,i_2,i_3,i_2,i_3,i_6}$ from equation (1) representing the refined potential energy function of H_3O^+ $V(r_1, r_2, r_3, \alpha_{12}, \alpha_{13}, \alpha_{23})$ are given in the supplementary material together with a Fortran program. It is expressed in terms of the valence coordinates r_i and α_{jk} independent from the special coordinate choice used in TROVE and thus can be used with any other programs. It should be noted, however, that because of the approximations used in TROVE (non-exact KEO, incomplete basis set etc., linearization of the valence coordinates in the representation of PES), the rovibrational energies obtained using our refined PES are expected to be somewhat different from ours.

The rovibrational energies and wavefunctions were computed variationally using the refined PES for $J = 0 \ldots 40$. The transitional intensities (Einstein A coefficients) were generated with our GPU code GAIN-MPI (Al-Refaie, Tennyson & Yurchenko 2017) in conjunction with the *ab initio* DMS described above.

5 LINE LIST

The rovibrational energies and Einstein A coefficients were then compiled into a line list eXeL utilizing the two-parts ExoMol format (Tennyson et al. 2016), consisting of state and transition files. The line list consists of 1173 114 states and 2089 331 073 transitions covering the energy

Table 1. A comparison of the calculated energy (Calc.) term values (cm^{-1}) of H_3O^+ with the experimental or empirically derived (Obs.) term values and band centres (cm^{-1}) for $J = 0$, 1, and 2. The complete table of the fitting set ($J = 0$, 1, 2, 3, 4, 6, 8, 10, and 16) is given in supplementary material.

J	Γ	State	Obs.	Calc.	Obs.-Calc.	J	Γ	State	Obs.	Calc.	Obs.-Calc.
0	A_1'	$g.s.$	0.0000	0.0000	0.0000	2	A_2'	ν_4^+	1669.0705	1669.0055	0.0649
0	A_1'	ν_2^+	581.1768	581.1194	0.0574	2	A_2'	ν_1^+	3584.6243	3584.5699	0.0544
0	A_1'	$2\nu_2^+$	1475.8400	1476.6341	– 0.7941	2	A_2'	ν_1^-	3634.4900	3634.5577	– 0.0677
0	A_1'	ν_1^+	3445.0024	3445.1247	– 0.1223	2	E'	$g.s.$	47.0775	47.0957	– 0.0182
0	E'	ν_4^+	1626.0202	1625.9707	0.0494	2	E'	ν_2^-	116.8069	116.8767	– 0.0698
0	E'	ν_3^+	3536.0364	3536.0017	0.0347	2	E'	ν_2^+	627.9416	627.9046	0.0370
0	A_2''	ν_2^-	55.3275	55.4027	– 0.0752	2	E'	$2\nu_2^-$	1014.1295	1014.1451	– 0.0156
0	A_2''	$2\nu_2^-$	954.3777	954.3953	– 0.0175	2	E'	ν_4^+	1695.4812	1695.4250	0.0561
0	A_2''	ν_1^-	3491.1533	3491.3405	– 0.1871	2	E'	ν_4^-	1754.2401	1754.3021	– 0.0619
0	E''	ν_4^-	1693.9311	1694.0408	– 0.1096	2	E'	ν_1^+	3491.5374	3491.6390	– 0.1017
0	E''	ν_3^-	3574.7899	3574.7419	0.0481	2	E'	ν_1^-	3551.8320	3551.9705	– 0.1386
1	A_2'	$g.s.$	22.4811	22.5019	– 0.0208	2	E'	ν_3^+	3580.6437	3580.6524	– 0.0088
1	A_2'	ν_2^+	603.5178	603.4797	0.0381	2	E'	ν_1^+	3602.1477	3602.1407	0.0070
1	A_2'	ν_4^-	1714.4010	1714.5415	– 0.1405	2	E'	ν_3^-	3636.3740	3636.3380	0.0361
1	A_2'	ν_1^+	3467.1385	3467.2640	– 0.1255	2	A_2''	ν_2^-	121.6192	121.6888	– 0.0696
1	A_2'	ν_3^-	3590.7923	3590.7246	0.0677	2	A_2''	$2\nu_2^-$	1018.5442	1018.5605	– 0.0164
1	E'	ν_2^-	72.6131	72.6866	– 0.0735	2	A_2''	ν_4^+	1693.3494	1693.2513	0.0982
1	E'	$2\nu_2^-$	971.3537	971.3701	– 0.0164	2	A_2''	ν_4^-	1736.1900	1736.2166	– 0.0266
1	E'	ν_4^+	1649.1761	1649.1168	0.0593	2	A_2''	ν_1^-	3556.5593	3556.6933	– 0.1340
1	E'	ν_4^-	1708.8804	1708.9578	– 0.0774	2	A_2''	ν_1^+	3596.1048	3596.0093	0.0955
1	E'	ν_1^-	3508.2267	3508.4025	– 0.1758	2	A_2''	ν_1^-	3623.3991	3623.3456	0.0535
1	E'	ν_1^+	3558.0829	3558.0571	0.0258	2	E''	$g.s.$	62.3662	62.3838	– 0.0176
1	E'	ν_3^-	3592.8914	3592.8400	0.0513	2	E''	ν_2^-	102.3574	102.4282	– 0.0709
1	A_2''	ν_4^+	1645.4437	1645.4003	0.0434	2	E''	ν_2^+	643.1580	643.1157	0.0423
1	A_2''	ν_1^+	3552.2612	3552.2819	– 0.0208	2	E''	$2\nu_2^-$	1000.8832	1000.8971	– 0.0138
1	E''	$g.s.$	17.3803	17.4012	– 0.0209	2	E''	ν_4^+	1687.7512	1687.6962	0.0550
1	E''	ν_2^+	598.4434	598.4071	0.0363	2	E''	ν_4^-	1746.3154	1746.4770	– 0.1616
1	E''	ν_4^+	1641.4819	1641.4223	0.0595	2	E''	ν_4^-	1762.0066	1762.1048	– 0.0982
1	E''	ν_4^-	1716.6186	1716.7175	– 0.0990	2	E''	ν_1^+	3506.4561	3506.5479	– 0.0918
1	E''	ν_1^+	3462.1613	3462.2898	– 0.1285	2	E''	ν_1^-	3537.6298	3537.7900	– 0.1603
1	E''	ν_3^+	3554.1949	3554.1491	0.0458	2	E''	ν_3^+	3598.2704	3598.2424	0.0280
1	E''	ν_1^-	3596.5379	3596.4975	0.0404	2	E''	ν_1^-	3640.0122	3639.9883	0.0239

range up to $hc \cdot 18\,000$ cm^{-1} and the wavenumber range up to 10 000 cm^{-1} with the lower energy value limited by $hc \cdot 10\,000$ cm^{-1}. The transitions are split into 100 Transition files of 100 cm^{-1} each. Extracts from the state and transition files are shown in Tables 2 and 3, illustrating their structure and quantum numbers. The rovibrational states of H_3O^+ are assigned with the following QNs: the total angular momentum J; the projection of J on the molecular axis k; the total, vibrational and rotational symmetries $\Gamma_{\rm tot}$, $G_{\rm vib}$ and $\Gamma_{\rm rot}$ in $\mathcal{D}_{3h}$(M), respectively; the local mode quantum numbers v_1, v_2, v_3 (stretches), v_4, v_5 (bends), and v_6 (inversion) in accordance with the corresponding vibrational primitive basis functions as described above and the normal mode QNs n_1, n_2, n_3, l_3, n_4, l_4.

In order to improve the quality of the line list further, the TROVE theoretical energies were replaced by the empirical values from Yu et al. (2009) where possible.

The fifth columns of the H_3O^+ states file contains the uncertainty (Yurchenko et al. 2020) of the corresponding term value (cm^{-1}), estimated using the following conservative criterion:

$$\sigma = 0.2\,n_1 + 0.2\,n_2 + 0.2\,n_3 + 0.2\,n_4 + 0.005\,J(J+1).$$

Only for the states replaced by empirical values, the empirical uncertainties by Yu et al. (2009) were used; these uncertainties are all significantly smaller than estimated uncertainties of our computed levels.

The rotation-vibrational ground state $J = 0$, ($n_1 = 0$, $n_2 = 0$, $n_3 = 0$, $n_4 = 0$) has the symmetry A_1' and therefore does not exist. The lowest existing rovibrational state is $J = 1$, $K = 1$ (E'') of (0,0,0,0) with the difference of $hc \cdot 17.3803$ cm^{-1} above the ground state. Following the same convention used for the BYTe line list for Ammonia (Yurchenko, Barber & Tennyson 2011), here we chose the zero-point energy (ZPE) of the state (0,0,0,0), $J = 0$, see Table 1, which we estimated as $hc \cdot 7436.6$ cm^{-1} relative to the minimum of the refined PES of H_3O^+. Therefore, the line intensities as well as partition functions were computed using this convention.

An overview of the absorption spectra at a range of temperatures is shown in Fig. 1. The spectra were computed using the eXeL line list on a grid of 1 cm^{-1} assuming a Gaussian line profile of half width at half-maximum (HWHM) of 1 cm^{-1}. The strongest band is ν_3 at 2.9 µm.

Table 2. Extract from the states file for the eXeL line list.

					Normal mode QN								Rot. QN			TROVE QN					
i	$\tilde{E}$	g_{tot}	J	Unc.	Γ	n_1	n_2	n_3	l_3	n_4	l_4	Γ_{vib}	K	Γ_{rot}	C_i	v_1	v_2	v_3	v_4	v_5	v_6
3476	22.481050	12	1	0.0000	A2’	0	0	0	0	0	0	A1’	0	A2’	1.00	0	0	0	0	0	0
3477	603.517820	12	1	0.0014	A2’	0	1	0	0	0	0	A1’	0	A2’	− 1.00	0	0	0	0	0	2
3478	1497.455621	12	1	0.41	A2’	0	2	0	0	0	0	A1’	0	A2’	1.00	0	0	0	0	0	4
3479	1714.401040	12	1	0.0025	A2’	0	0	0	0	1	1	E’	1	E’	1.00	0	0	0	0	1	1
3480	2621.469120	12	1	0.41	A2’	0	2	0	0	0	0	E’	1	E’	1.00	0	0	0	0	1	3
3481	2692.172161	12	1	0.41	A2’	0	1	0	0	1	1	A1’	0	A2’	− 1.00	0	0	0	0	0	6
3482	3237.598553	12	1	0.41	A2’	0	1	0	0	1	1	A1’	0	A2’	− 1.00	0	0	0	0	2	0
3483	3336.105179	12	1	0.61	A2’	0	2	0	0	1	1	E’	1	E’	− 1.00	0	0	0	0	2	1
3484	3467.138460	12	1	0.0036	A2’	0	0	0	0	2	0	A1’	0	A2’	1.00	0	0	1	0	0	0
3485	3590.792340	12	1	0.0012	A2’	0	0	0	0	2	0	E’	1	E’	1.00	0	1	0	0	0	1
3486	3735.190221	12	1	0.41	A2’	0	0	0	0	2	2	E’	1	E’	− 1.00	0	0	0	0	1	5
3487	3820.010491	12	1	0.41	A2’	0	0	0	0	2	2	A1’	0	A2’	1.00	0	0	0	0	2	2
3488	4049.835413	12	1	0.21	A2’	1	0	0	0	0	0	A1’	0	A2’	− 0.99	0	0	1	0	0	2

Notes. i: State counting number.
$\tilde{E}$: State energy term value in cm^{-1}.
g_{tot}: Total state degeneracy.
J: Total angular momentum.
unc.: Uncertainty cm^{-1}.
Γ: Total symmetry index in $\mathcal{D}_{3\mathrm{h}}$(M)
n_1: Normal mode stretching symmetry (A_1') QN.
n_2: Normal mode inversion (A_2'') QN.
n_3: Normal mode stretching asymmetric (E') QN.
l_3: Normal mode stretching angular momentum QN.
n_4: Normal mode bending asymmetric (E') QN.
l_4: Normal mode bending angular momentum QN.
Γ_{vib}: Vibrational symmetry index in $\mathcal{D}_{3\mathrm{h}}$(M)
K: Projection of J on molecular symmetry axis.
Γ_{rot}: Rotational symmetry index in $\mathcal{D}_{3\mathrm{h}}$(M).
C_i: Coefficient with the largest contribution to the ($J = 0$) contracted set; $C_i \equiv 1$ for $J = 0$.
TROVE (local mode) QNs:
v_1–v_3: Stretching QNs.
v_4, v_5: Asymmetric bending QNs.
v_6: Inversion QN.

Table 3. Extract from the transitions file for the eXeL line list.

f	i	A_{fi}
9135	4964	9.4529E-06
3483	2058	1.9377E-04
2590	4967	3.1507E-05
9141	4967	1.1550E-04
9142	1033	1.4600E-02
4975	9135	2.1565E-04
3484	7754	4.0709E-02
9142	4968	2.3899E-02
4979	2589	2.7283E-04
9147	4969	3.8512E-04

Notes. f: Upper state counting number.
i: Lower state counting number.
A_{fi}: Einstein A coefficient in s^{-1}.

Table 4 lists vibrational transition moments for several of the strongest bands of H_3O^+ computed using the eXeL line list and Fig. 2 illustrates five main fundamental and overtone bands at $T = 296$ K in absorption.

An eXeL partition function was computed on a 1 K grid of temperatures up to $T = 1500$ K. Fig. 3 compares this partition function with that by Irwin (1988) produced for JANAF polyatomic molecules. The latter had to be multiplied by 10 in order to get best agreement with ExoMol which follows HITRAN’s convention (Gamache et al. 2017) of using the full nuclear spin multiplicities.

In order to estimate the effect of the energy threshold of 10 000 cm^{-1} in the completeness of the line list for different ratio, we have computed a partition function of H_3O^+ using energies below 10 000 cm^{-1}, $Q^{10\,000}(T)$ and compared to that of the complete partition function $Q^{18\,000}(T)$ (here approximated by the energies below 18 000 cm^{-1}). Fig. 4 shows a ratio $Q^{10\,000}(T)/Q^{18\,000}(T)$ of the partition functions. At $T = 1550$ K, the partition function of H_3O^+ should be 98 per cent complete.

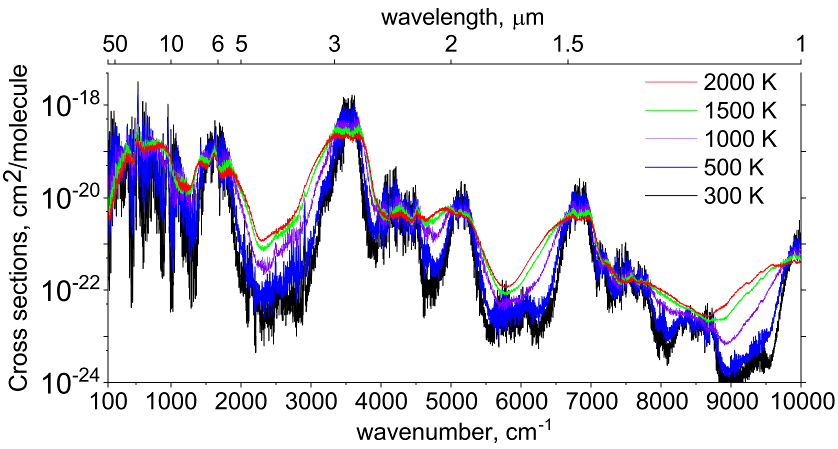

Figure 1. Temperature dependence of the H_3O^+ absorption spectrum: the spectrum becomes flatter with increasing temperature. The spectrum was computed using the Gaussian line profile with HWHM of 1 cm^{-1}.

Table 4. Vibrational transition moments (Debye) $\bar{\mu}$ and band centres $\tilde{\nu}$ for selected bands of H_3O^+ originated from the two components of the ground state, 0^+ and 0^- and computed using eXeL.

Band	$\tilde{\nu}$ (cm^{-1})	$\bar{\mu}$ (Debye)
0^-	55.403	1.4375
$\nu_2^+ - 0^-$	525.717	0.7337
$2\nu_2^-$	954.395	0.2888
$3\nu_2^+ - 0^-$	1421.231	0.1038
ν_4^+	1625.971	0.2307
$\nu_4^- - 0^-$	1638.638	0.2241
$2\nu_4^{0+}$	3240.946	0.0431
$2\nu_4^{0-} - 0^-$	3267.694	0.0482
$\nu_1^+ - 0^-$	3389.722	0.0505
ν_1^-	3491.340	0.0460
ν_3^+	3536.002	0.3326
$\nu_3^- - 0^-$	3519.339	0.3274

6 H_3O^+ IN PLANETARY ATMOSPHERES AND COOL STARS

For many years, H_3O^+ has been considered as an important ion in the atmospheres of giant planets where O-rich materials are being deposited (see Moses & Bass 2000). In 2011, O'Donoghue et al. (2013) detected a series of 'peaks and troughs' in the pole-to-pole H_3^+ emission spectrum of Saturn, redetecting these features in 2013 (O'Donoghue et al. 2017). These features corresponded to locations where magnetic field lines passing through the planet's rings connected to the upper atmosphere. O'Donoghue et al. (2017) explained the peaks as being formed because water-derived ions from the rings were soaking up electrons in the northern mid-latitude ionosphere, reducing the rate of H_3^+ dissociative recombination and consequently producing a relative local increase in this ion's density. At southern mid-latitudes, however, the influx of water was sufficiently large to overwhelm this effect and produce a local minimum of H_3^+ as a result of proton-hopping:

$$H_3^+ + H_2O \rightarrow H_2 + H_3O^+. \tag{17}$$

Making use of modelling by Moore et al. (2015), O'Donoghue et al. (2019) deduced that the rings of Saturn would be fully eroded in between 168 and 1110 Myr time at the current rate of water deposition.

A much larger equatorial mass influx from Saturn's rings, primarily composed of neutral nanograins, was discovered by the Cassini spacecraft during its end-of-mission proximal orbits (Hsu et al. 2018; Mitchell et al. 2018; Waite et al. 2018). Such a large mass-loss from the rings could imply an even shorter lifetime, or perhaps a highly temporally variable process (Perry et al. 2018), though it is clear that deducing the lifetime of Saturn's rings from such limited measurements warrants caution (e.g. Crida et al. 2019).

Moore et al. (2018) have analysed data from the final orbits of the Cassini spacecraft and deduced that molecular ions with a mean mass of 11 Daltons dominate Saturn's lower ionosphere in the planet's equatorial regions, within the range derived from observations by the Cassini spacecraft (Morooka et al. 2018; Wahlund et al. 2018). The model of Moore et al. (2018) produces an H_3O^+ density of 10^9 m^{-3} at an altitude around 1500 km.

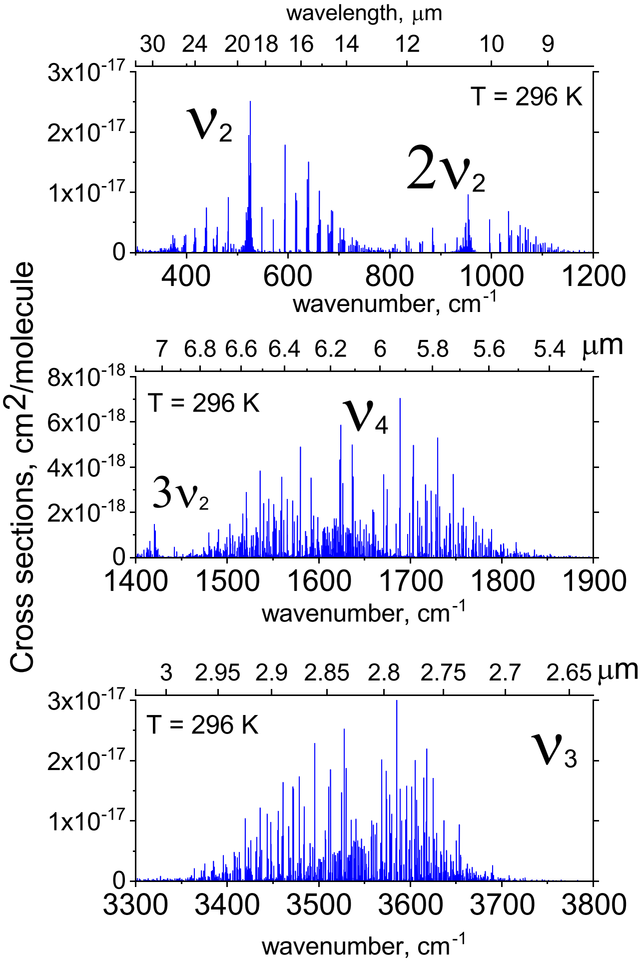

Figure 2. Fundamental and overtone bands of H_3O^+ in absorption at $T = 296$ K computed using the eXeL line list and the Doppler line profile.

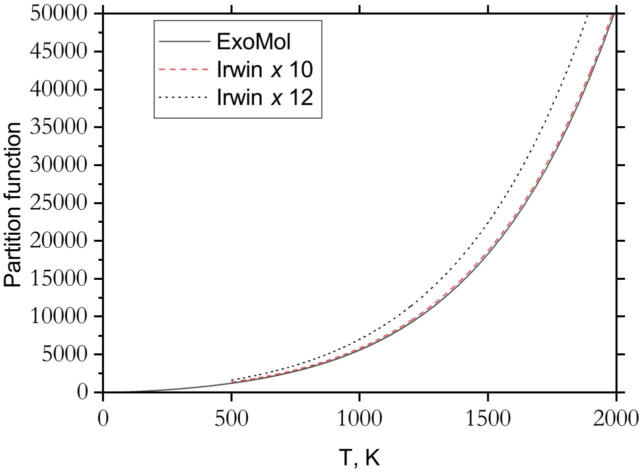

Figure 3. Partition functions of H_3O^+ computed using eXeL energies and constants provided by Irwin (1988).

Fig. 5 shows an H_3O^+ emission spectrum of Saturn's equator, where H_3O^+ is expected to be as large as $N \sim 1.2 \times 10^{15}$ m^{-2} (Moore et al. 2018), modelled using this line list. The temperature is assumed to be $T = 370$ K, reasonable for Saturn's equatorial ionosphere (Yelle et al. 2018; Brown et al. 2020). The possibility of making a detection from a ground-based infrared observatory is demonstrated by comparing this figure with a transmission spectrum of the terrestrial atmosphere at the summit of Maunakea, Hawai'i, using the data provided by the Gemini Observatory.[1]

---

[1] https://www.gemini.edu/sciops/telescopes-and-sites/observing-condition-constraints/ir-transmission-spectra

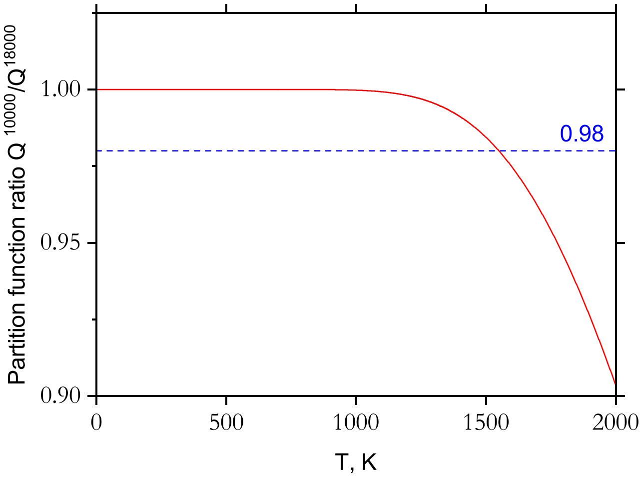

Figure 4. Ratio of two partition functions of H_3O^+, $Q^{10\,000}$ (computed using all energies below $hc \cdot 10\,000$ cm^{-1}) and $Q^{18\,000}$ (computed using all energies below $hc \cdot 18\,000$ cm^{-1}).

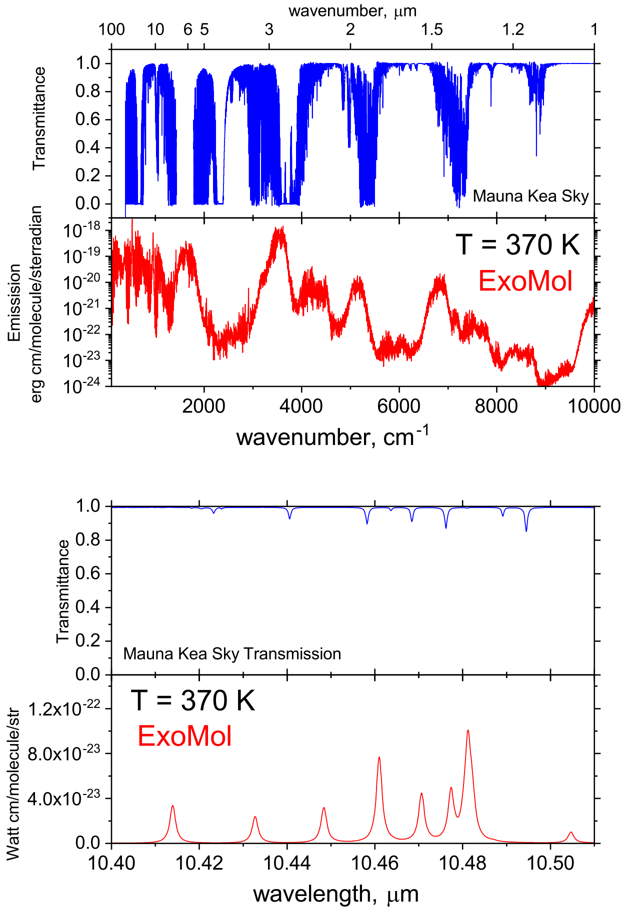

Figure 5. Spectrum of H_3O^+ at $T = 370$ K (top: emission cross-sections; bottom: emission-line intensities) together with a spectrum of the Earth atmosphere at Mauna Kea (water vapour column 1.0 mm and airmass = 1) www.gemini.edu. The H_3O^+ spectrum was simulated assuming a Doppler line profile in air. The H_3O^+ line positions were redshifted by an equivalent of 20 km s^{-1}.

In particular, in Fig. 5, we identify a spectral 'window' around 10.40–10.50 μm where a blend of H_3O^+ lines are clear of atmospheric absorption, even more so because we have included a redshift of Saturn's spectrum equivalent to 20 km s^{-1}, such as would be the typical case a few months past opposition as the planet recedes. This spectrum has been generated using a spectral resolving power $\lambda/\Delta\lambda = 85\,000$, the resolving power of the TEXES mid-infrared spectrometer (Lacy et al. 2000) which is often used by telescopes belonging to the Mauna Kea Observatory group. Based on Fig. 5, this spectral region is extremely promising for the first detection of H_3O^+ in a planetary atmosphere.

As well as the Solar system's giant planets, there is now considerable interest in determining the composition of giant exoplanet atmospheres and those of cool stars. Recently, Helling & Rimmer (2019) have discussed the possibility of detecting H_3O^+ in exoplanets and brown dwarf stars. They modelled the atmosphere of an M8.5 dwarf with an effective temperature of 2600 K. Their model indicated that the H_3O^+ density is likely to be $\geq 10^{11}$ m^{-3} throughout the pressure range from 1 bar to 1 μbar, and considerable proportion of the star's atmosphere. They concluded that this class of star could be a target for high-temperature H_3O^+ emission in future studies: this could particularly be the case with the launch of the *James Webb Space Telescope* and its MIRI instrument (see e.g. Marini et al. 2020). Bourgalais et al. (2020) have also suggested that H_3O^+ could be detectable in the observational spectra of sub-Neptunes and proposed H_3O^+ ions as potential biomarkers for Earth-like planets.

7 CONCLUSION

A new hot line list eXeL for H_3O^+ is presented. The line list covers the wavenumber rage up to 10 000 cm^{-1} (wavelengths >1 μm) with the rotational excitation of $J = 0$–40. The eXeL line list should be applicable for the temperatures up to 1500 K. There is evidence that this ion should be detectable in Solar system gas giants, exoplanets and brown dwarfs. The eXeL provides the spectroscopic data necessary for such detections to be attempted.

Our line list for H_3O^+ is aimed to help realistic simulations of absorption and emission properties of atmospheres of (exo-)planets and brown dwarfs as well as of cometary comae and interstellar clouds, their retrials and detections of H_3O^+.

ExoMol project originally concentrated on providing line lists for neutral molecules. At present, the data base contains line lists for a number of ions of (possible) importance for studies of the early Universe, namely HD^+ (Amaral et al. 2019), HeH^+ (Engel et al. 2005; Amaral et al. 2019), LiH^+ (Coppola, Lodi & Tennyson 2011), H_2D^+ (Sochi & Tennyson 2010), and H_3^+ (Mizus et al. 2017). For ions important in (exo-)planetary atmosphere, the data base so far only contains line lists for H_3^+ and OH^+ (Bernath 2020; Wang, Tennyson & Yurchenko 2020). The current H_3O^+ line list represents an important addition to this and we are in the process of adding other ions, starting with HCO^+.

The line lists can be downloaded from the CDS (http://cdsweb.u-strasbg.fr/) or from ExoMol (www.exomol.com) data bases.

ACKNOWLEDGEMENTS

This work was supported by the STFC Projects No. ST/M001334/1 and ST/R000476/1. The authors acknowledge the use of the UCL Legion High Performance Computing Facility (Legion@UCL) and associated support services in the completion of this work, along with the Cambridge Service for Data Driven Discovery (CSD3), part of which is operated by the University of Cambridge Research Computing on behalf of the STFC DiRAC HPC Facility (www.dirac.ac.uk). The DiRAC component of CSD3 was funded by BEIS capital funding via STFC capital grants ST/P002307/1 and ST/R002452/1 and STFC operations grant ST/R00689X/1. DiRAC is part of the National e-Infrastructure.

DATA AVAILABILITY STATEMENT

Full data are made available. The line lists can be downloaded from the CDS (http://cdsweb.u-strasbg.fr/) or from ExoMol (www.exomol.com) data bases. The following files are available as supplementary information:

H3Op_PES_refined.inp	Input file for HO3p_PES.f90 containing the potential parameters defining refined PES of H_3O^+
HO3p_PES.f90	Fortran 90 routine for calculating potential energy values in combination with the input file H3Op_PES_refined.inp
H3Op_DMS.inp	Input file for H3Op_DMS.f90 containing dipole moment parameters defining ab initio DMS of H_3O^+
H3Op_DMS.f90	Fortran 90 routine for calculating dipole momment values in combination with the input file H3Op_DMS.inp

REFERENCES

Al-Refaie A. F., Yurchenko S. N., Tennyson J., 2017, Comput. Phys. Commun., 214, 216
Amaral P. H. R., Diniz L. G., Jones K. A., Stanke M., Alijah A., Adamowicz L., Mohallem J. R., 2019, ApJ, 878, 95
Andersen L. H., Heber O., Kella D., Pedersen H. B., Vejby-Christensen L., Zajfman D., 1996, Phys. Rev. Lett., 77, 4891
Araki M., Ozeki H., Saito S., 1999, Mol. Phys., 97, 177
Balsiger H. et al., 1986, Nature, 321, 330
Barber R. J., Miller S., Stallard T., Tennyson J., Hirst P., Carroll T., Adamson A., 2007, Icarus, 187, 167
Begemann M. H., Saykally R. J., 1985, J. Chem. Phys., 82, 3570
Begemann M. H., Gudeman C. S., Pfaff J., Saykally R. J., 1983, Phys. Rev. Lett., 51, 554
Bernath P. F., 2020, J. Quant. Spectrosc. Radiat. Transfer, 240, 106687
Bogey M., Demuynck C., Denis M., Destombes J. L., 1985, A&A, 148, L11
Botschwina P., Rosmus P., Reinsch E.-A., 1983, Chem. Phys. Lett., 102, 299
Bourgalais J. et al., 2020, ApJ, 895, 77
Brown Z., Koskinen T., Müller-Wodarg I., West R., Jouchoux A., Esposito L., 2020, Nat. Astron., 1
Buhr H. et al., 2010, Phys. Rev. Lett., 105, 103202
Bunker P. R., Jensen P., 1998, Molecular Symmetry and Spectroscopy, 2nd edn. NRC Research Press, Ottawa
Bunker P. R., Amano T., Špirko V., 1984, J. Mol. Spectrosc., 107, 208

Chaban G. M., Jung J. O., Gerber R. B., 2000, J. Phys. Chem. A, 104, 2772
Coles P. A., Yurchenko S. N., Tennyson J., 2019, MNRAS, 490, 4638
Cooley J. W., 1961, Math. Comp., 15, 363
Coppola C. M., Lodi L., Tennyson J., 2011, MNRAS, 415, 487
Cranfield C. G. et al., 2016, Langmuir, 32, 10725
Crida A., Charnoz S., Hsu H.-W., Dones L., 2019, Nat. Astron., 3, 967
Dalgarno A., Black J. H., 1976, Rep. Prog. Phys., 39, 573
Davies P. B., Johnson S. A., Hamilton P. A., 1984, A&A, 141, L9
Davies P. B., Johnson S. A., Hamilton P. A., Sears T. J., 1986, Chem. Phys., 108, 335
Dong F., Nesbitt D. J., 2006, J. Chem. Phys., 125, 144311
Dunning T. H., 1989, J. Chem. Phys., 90, 1007
Dunning T. H., Peterson K. A., Wilson A. K., 2001, J. Chem. Phys., 114, 9244
Endres C. P., Schlemmer S., Schilke P., Stutzki J., Müller H. S. P., 2016, J. Mol. Spectrosc., 327, 95
Engel E. A., Doss N., Harris G. J., Tennyson J., 2005, MNRAS, 357, 471
Ermoshin V. A., Sobolewski A. L., Domcke W., 2002, Chem. Phys. Lett., 356, 556
Ferguson W. I., Handy N. C., 1980, Chem. Phys. Lett., 71, 95
Furuya T., Saito S., 2008, J. Chem. Phys., 128, 034311
Gamache R. R. et al., 2017, J. Quant. Spectrosc. Radiat. Transfer, 203, 70
Gerin M. et al., 2010, A&A, 518, L110
Goicoechea J. R., Cernicharo J., 2001, ApJ, 554, L213
González-Alfonso E. et al., 2013, A&A, 550, A25
Gruebele M., Polak M., Saykally R. J., 1987, J. Chem. Phys., 87, 3347
Haese N. N., Liu D. J., Oka T., 1988, J. Mol. Spectrosc., 130, 262
Hasse N. N., Oka T., 1984, J. Chem. Phys., 80, 572
Helling C., Rimmer P. B., 2019, Phil. Trans. R. Soc. A, 377, 20180398
Ho W. C., Pursell C. J., Oka T., 1991, J. Mol. Spectrosc., 149, 530
Hollenbach D., Kaufman M. J., Neufeld D., Wolfire M., Goicoechea J. R., 2012, ApJ, 754, 105
Hollis J. M., Churchwell E. B., Herbst E., De Lucia F. C., 1986, Nature, 322, 524
Hougen J. T., Bunker P. R., Johns J. W. C., 1970, J. Mol. Spectrosc., 34, 136
Hsu H.-W. et al., 2018, Science, 362, aat3185
Huang X., Carter S., Bowman J., 2003, J. Chem. Phys., 118, 5431
Indriolo N. et al., 2015, ApJ, 800, 40
Irwin A. W., 1988, A&AS, 74, 145
Jensen M. J., Bilodeau R. C., Safvan C. P., Seiersen K., Andersen L. H., Pedersen H. B., Heber O., 2000, ApJ, 543, 764
Kendall R. A., Dunning T. H., Harrison R. J., 1992, J. Chem. Phys., 96, 6796
Kozlov M. G., Levshakov S. A., 2010, ApJ, 726, 65
Lacy J. H., Richter M. J., Greathouse T. K., Jaffe D. T., 2000, American Astronomical Society Meeting Abstracts #197 . p. 15.09
Lemoine B., Destombes J. L., 1984, Chem. Phys. Lett., 111, 284
Lis D. C. et al., 1997, AAS/Division for Planetary Sciences Meeting Abstracts #29 . p. 37.02
Lischka H., Dyczmons V., 1973, Chem. Phys. Lett., 23, 167
Liu D. J., Oka T., 1985, Phys. Rev. Lett., 54, 1787
Liu D. J., Oka T., Sears T. J., 1986, J. Chem. Phys., 84, 1312
Mann J. E., Xie Z., Savee J. D., Bowman J. M., Continetti R. E., 2013, J. Phys. Chem. A, 117, 7256
Marini E. et al., 2020, MNRAS, 493, 2996
Martinez R. et al., 2019, J. Phys. Chem. A, 123, 8001
Mehringer D. et al., 1997, IAU Circ., 6625, 1
Melnikov V. V., Yurchenko S. N., Tennyson J., Jensen P., 2016, Phys. Chem. Chem. Phys., 18, 26268
Millar T. J., Defrees D. J., McLean A. D., Herbst E., 1988, A&A, 194, 250
Mitchell D. G. et al., 2018, Science, 362, eaat2236
Mizus I. I., Alijah A., Zobov N. F., Lodi L., Kyuberis A. A., Yurchenko S. N., Tennyson J., Polyansky O. L., 2017, MNRAS, 468, 1717
Moore L., O'Donoghue J., Müller-Wodarg I., Galand M., Mendillo M., 2015, Icarus, 245, 355
Moore L. et al., 2018, Geophys. Res. Lett., 45, 9398
Morooka M. W., Wahlund J.-E., Andrews D. J., Persoon A. M., Ye S.-Y., Kurth W. S., Gurnett D. A., Farrell W. M., 2018, J. Geophys. Res.: Space, 123, 4668
Moses J. I., Bass S. F., 2000, J. Geophys. Res., 105, 7013
Müller H. S. P., Dong F., Nesbitt D. J., Furuya T., Saito S., 2010, Phys. Chem. Chem. Phys., 12, 8362
Neau A. et al., 2000, J. Chem. Phys., 113, 1762
Noumerov B. V., 1924, MNRAS, 84, 592
Novotny O. et al., 2010, J. Phys. Chem. A, 114, 4870
O'Donoghue J., Stallard T. S., Melin H., Jones G. H., Cowley S. W. H., Miller S., Baines K. H., Blake J. S. D., 2013, Nature, 496, 193
O'Donoghue J., Moore L., Connerney J. E. P., Melin H., Stallard T. S., Miller S., Baines K. H., 2017, Geophys. Res. Lett., 44, 11,762
O'Donoghue J., Moore L., Connerney J., Melin H., Stallard T. S., Miller S., Baines K. H., 2019, Icarus, 322, 251
Okumura M., Yeh L. I., Myers J. D., Lee Y. T., 1990, J. Chem. Phys., 94, 3416
Owens A., Yurchenko S. N., Polyansky O. L., Ovsyannikov R. I., Thiel W., Špirko V., 2015, MNRAS, 454, 2292
Perry M. E. et al., 2018, Geophys. Res. Lett., 45, 10093
Petek H., Nesbitt D. J., Owrutsky J. C., Gudeman C. S., Yang X., Harris D. O., Moore C. B., Saykally R. J., 1990, J. Chem. Phys., 92, 3257
Petit A. S., Wellen B. A., McCoy A. B., 2012, J. Chem. Phys., 136, 074101
Phillips T. G., van Dishoeck E. F., Keene J., 1992, ApJ, 399, 533
Pickett H. M., 1991, J. Mol. Spectrosc., 148, 371

Pickett H. M., Poynter R. L., Cohen E. A., Delitsky M. L., Pearson J. C., Müller H. S. P., 1998, J. Quant. Spectrosc. Radiat. Transfer, 60, 883
Plummer G. M., Herbst E., de Lucia F. C., 1985, J. Chem. Phys., 83, 1428
Rajamäki T., Miani A., Halonen L., 2003, J. Chem. Phys., 118, 10929
Rajamäki T., Noga J., Valiron P., Halonen L., 2004, Mol. Phys., 102, 2259
Rauer H., 1997, Earth Moon Planets, 79, 161
Roy S., Dang L. X., 2015, Chem. Phys. Lett., 628, 30
Rubin M., Hansen K. C., Gombosi T. I., Combi M. R., Altwegg K., Balsiger H., 2009, Icarus, 199, 505
Rui Z., Rui-Bo W., Song L., Guang-Ming H., Chuan-Xi D., 2007, Chin. Phys. Lett., 24, 2569
Sánchez Contreras C. et al., 2015, A&A, 577, A52
Sears T. J., Bunker P. R., Davies P. B., Johnson S. A., Špirko V., 1985, J. Chem. Phys., 83, 2676
Sochi T., Tennyson J., 2010, MNRAS, 405, 2045
Spanel P., Spesyvyi A., Smith D., 2019, Anal. Chem., 91, 5380
Špirko V., Bunker P. R., 1982, J. Mol. Spectrosc., 95, 226
Stahn A., Solka H., Adams H., Urban W., 1987, Mol. Phys., 60, 121
Stephenson S. K., Saykally R. J., 2005, Chem. Rev., 105, 3220
Tan J. A., Li J.-W., Chiu C.-c., Liao H.-Y., Huynh H. T., Kuo J.-L., 2016, Phys. Chem. Chem. Phys., 18, 30721
Tang J., Oka T., 1999, J. Mol. Spectrosc., 196, 120
Tennyson J., Yurchenko S. N., 2012, MNRAS, 425, 21
Tennyson J. et al., 2016, J. Mol. Spectrosc., 327, 73
Timmermann R., Nikola T., Poglitsch A., Geis N., Stacey G. J., Townes C. H., 1996, ApJ, 463, L109
Tran T. D., Rednyk S., Kovalenko A., Roučka Š., Dohnal P., Plašil R., Gerlich D., Glosík J., 2018, ApJ, 854, 25
Uy D., White E. T., Oka T., 1997, J. Mol. Spectrosc., 183, 240
Verhoeve P., Termeulen J. J., Meerts W. L., Dymanus A., 1988, Chem. Phys. Lett., 143, 501
Verhoeve P., Versluis M., Termeulen J. J., Meerts W. L., Dymanus A., 1989, Chem. Phys. Lett., 161, 195
Wahlund J.-E. et al., 2018, Science, 359, 66
Waite J. H. et al., 2018, Science, 362, eaat2382
Wang Y., Tennyson J., Yurchenko S. N., 2020, Atoms, 8, 7
Werner H.-J., Knowles P. J., Knizia G., Manby F. R., Schütz M., 2012, WIREs Comput. Mol. Sci., 2, 242
Woon D. E., Dunning T. H., 1993, J. Chem. Phys., 98, 1358
Wootten A., Boulanger F., Bogey M., Combes F., Encrenaz P. J., Gerin M., Ziurys L., 1986, A&A, 166, L15
Wootten A., Mangum J. G., Turner B. E., Bogey M., Boulanger F., Combes F., Encrenaz P. J., Gerin M., 1991, ApJ, 380, L79
Yelle R. V., Serigano J., Koskinen T. T., Hörst S. M., Perry M. E., Perryman R. S., Waite J. H., Jr, 2018, Geophys. Res. Lett., 45, 10,951
Yu Q., Bowman J. M., 2016, J. Chem. Theory Comput., 12, 5284
Yu S., Drouin B. J., Pearson J. C., Pickett H. M., 2009, ApJS, 180, 119
Yurchenko S. N., Bunker P. R., Jensen P., 2005a, J. Mol. Struct., 742, 43
Yurchenko S. N., Zheng J. G., Lin H., Jensen P., Thiel W., 2005b, J. Chem. Phys., 123, 134308
Yurchenko S. N., Thiel W., Jensen P., 2007, J. Mol. Spectrosc., 245, 126
Yurchenko S. N., Barber R. J., Yachmenev A., Thiel W., Jensen P., Tennyson J., 2009, J. Phys. Chem. A, 113, 11845
Yurchenko S. N., Barber R. J., Tennyson J., 2011, MNRAS, 413, 1828
Yurchenko S. N., Yachmenev A., Ovsyannikov R. I., 2017, J. Chem. Theory Comput., 13, 4368
Yurchenko S. N., Mellor T. M., Freedman R. S., Tennyson J., 2020, MNRAS, 496, 5282

SUPPORTING INFORMATION

Supplementary data are available at *MNRAS* online.

H3Op_DMS.f90
H3Op_DMS.inp
H3Op_PES_refined.inp
HO3p_PES.f90

This paper has been typeset from a TEX/LATEX file prepared by the author.